

Part Four

**Most Common Diseases: Caries, Musculoskeletal Diseases,
Incontinence, Allergies**

12

Revealing the Nano-Architecture of Human Hard and Soft Tissues by Spatially Resolved Hard X-Ray Scattering

Hans Deyhle and Bert Müller

University of Basel, Department of Biomedical Engineering, Biomaterials Science Center,
Gewerbstrasse 14, 4123 Allschwil, Switzerland

12.1

Introduction

Human tissues are highly organized anisotropic structures, hierarchically ordered from the macroscopic down to the nanometer scale. These biologically generated materials are usually highly specialized and often provide a unique performance for the period of several decades. For example, human enamel consists of ordered hydroxyapatite crystallites organized in a fibrous continuum. The highly anisotropic organization and interaction of these components makes human enamel about three times tougher than its geological counterpart and much less brittle than sintered hydroxyapatite [1]. It is therefore of interest, to understand the synergetic structure of such tissues.

For this purpose, hard X-rays are of particular interest, because the deep penetration allows nondestructively probing the interior of specimens close to physiological conditions.

Radiography has been available for more than a century. Medical doctors routinely use this modality to image human tissues. Computed tomography (CT), or more precisely hard X-ray tomography in absorption contrast mode, has been implemented in daily clinical diagnosis. In both cases, the attenuation of the X-ray beam intensity traversing the tissues is measured. Because of the relatively low X-ray attenuation by the soft tissue components, the hard X-ray techniques concentrate on imaging hard tissues such as bone and tooth crowns. More recently, hard X-ray imaging techniques in phase contrast mode became available, which are much better suitable for the investigation of soft tissue components owing to their increased sensitivity for materials with low atomic numbers including carbon. These sophisticated methods allow detecting the phase shift generally described by the real part of the refractive index.

The spatial resolution of the real-space imaging techniques is ultimately limited by the wavelength of the probe. Hard X-rays have a wavelength of the order

of 0.1 nm. The spatial resolution of CT and radiography, however, is not better than a fraction of a micrometer, if one sets special X-ray optics aside. These contemporary real-space imaging techniques gave the possibility to image individual human cells [2,3].

Subcellular components, that is, anatomical structures on the true nanometer level are commonly imaged using electron microscopy. These experiments need high-vacuum conditions and, thus, a specimen preparation procedure that transforms the tissues into states far from physiological conditions. As the electrons strongly interact with matter, the imaging restricts to surfaces or thin sections of the human tissue.

For about a century, we know that X-rays can reveal atomic structures. X-ray scattering allows for the exact determination of arrangements from periodic features on the nanometer scale. It has been shown that the minerals in bones and teeth as well as the myelin sheaths in human brain tissues and collagen fibers of cartilage give rise to such periodicities and the related signals in scattering pattern. X-ray scattering has found increasing application in the medical research for the characterization of the nanoarchitecture of tissues and their components. Its combination with two-dimensional scanning allows mapping quantities as nanoscale anisotropy or preferential orientation over macroscopic specimens with micrometer resolution [4,5]. The present chapter introduces the experimental principles and selected applications in studying soft and hard tissues, that is, the breast, brain, parts of joints, and tooth crowns.

12.2

Spatially Resolved Hard X-Ray Scattering

12.2.1

Introductory Remarks on X-Ray Scattering

As X-ray diffraction, the X-ray scattering techniques belong to the reciprocal space or k -space, as they are based on an inverse relationship between the angles of X-rays scattered by the tissues and real-space nanometer periodicities of the tissues.

One can distinguish between two experimental setups: X-ray diffraction, or *wide-angle X-ray scattering* (WAXS), which is used to gain insight about the atomic lattice structure of crystals or crystallites, and *small-angle X-ray scattering* (SAXS), which deals with structures between 1 and several 100 nm. The underlying physical principles, however, are the same. The X-rays impinging on the tissues excite electrons, which in return emit secondary waves that interfere with each other [6]. The scattered waves are coherent, and their amplitudes add linearly. Depending on the tissue morphology, constructive interference occurs at well-defined angles. By measuring these angles, information about the relative positions of the electrons can be derived. It should be noted that one can restrict the description on coherent scattering, since at small angles the incoherent portion is negligible [6].

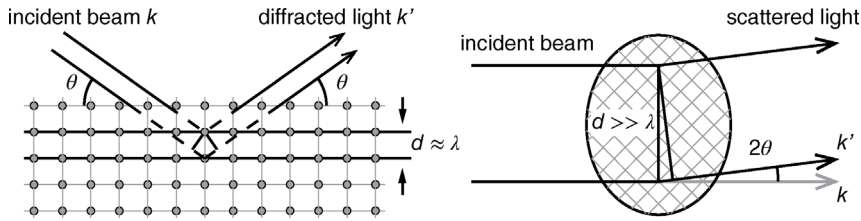


Figure 12.1 Reciprocal relationship between scattering angle and scattering feature dimension. At dimension d close to the wavelength of the X-rays, the electrons can be considered to be located at the position of the atoms, and information about the lattice structure of the

specimen is obtained at large angles. At dimensions d significantly larger than the wavelength, small-angle scattering occurs, providing information about the electron density distribution.

Within crystals the electrons are localized at the atoms. The relation between the crystallographic structure and the scattering angle can be described by the Bragg equation

$$\lambda = 2d \sin \theta, \quad (12.1)$$

where λ denotes the wavelength of the X-rays, d the spacing between atomic lattice planes, and θ the scattering angle, under which constructive interference occurs (cf. Figure 12.1). If the size of the inspected structures is of the order of magnitude of the X-ray wavelength, as is the case for crystal lattices, the scattering angles will be large, and the technique is termed WAXS. Diffraction peaks appear, when the Bragg equation is satisfied.

By collecting the positions of several diffraction peaks and comparing them with crystallographic databases, it is possible to reconstruct the lattice structure of the investigated crystal. It should be noted that the position of the diffraction peaks depends on crystal orientation; they lay in a plane parallel to the direction of the incident X-rays and perpendicular to the related lattice planes. Therefore, in anisotropic specimens, diffraction also provides information about crystal orientation.

If the dimension d of the investigated objects becomes much larger than the wavelength, the scattering angle will conversely get small (cf. Figure 12.1). When observing objects orders of magnitude larger than the atomic scale, it is practical to consider the electron density distribution $\rho(x)$, that is, the number of electrons per unit volume, rather than electrons localized at defined positions. Then, all electrons contribute to the scattering, and the scattered signal is the superposition of all contributions. If a specimen presents a homogeneous electron density, the individual contributions will cancel each other out. Thus, small-angle scattering only occurs when electron density inhomogeneity in the nanometer range exists. Since the scattering angle is dependent on the wavelength λ of the incident X-rays, it is useful and common to introduce the scattering vector or momentum transfer q , defined as

$$q = \frac{4\pi}{\lambda} \sin \theta = \frac{2\pi}{\lambda} |\mathbf{k}' - \mathbf{k}|, \quad (12.2)$$

where θ indicates the scattering angle. \mathbf{k} and \mathbf{k}' are unit vectors in the direction of the incoming and outgoing waves, respectively [6] (cf. Figure 12.1).

The resulting scattered amplitude A is then given by integrating over the contribution from all electrons as

$$A(q) = \int dV \cdot \rho(r)e^{-iqr}, \quad (12.3)$$

when the observer is located at distances much greater than the specimen size. Note that in experiments, the intensity $I(q)$ is recorded. This implies that the phase information is lost, making a back transform of the recorded intensities to the electron density distribution impossible. Thus, only derived quantities can be obtained from diffraction or scattering patterns. For a thorough treatment of SAXS formalism, see references [6,7].

12.2.2

Experimental Setup for X-Ray Scattering

The scheme of a scattering experiment can be described as follows. A narrow incident beam impinges on the specimen, where the X-rays interact with the electrons, and the scattered intensity is collected some distance away. The precise distance between specimen and detector can be obtained by measuring standards with well-known periodicities, for example, silver behenate (<http://www.esrf.eu/UsersAndScience/Experiments/CRG/BM26/SaxsWaxs/Silverbehenate>).

Only a fraction of the incoming photons are scattered, the majority is either absorbed in the specimen or transmitted. The transmitted, or direct, beam is generally collected by a beamstop in front of the detector. This allows tuning the sensitivity of the detector to the intensity of the SAXS signal and avoiding possible damage to the detector. It should be noted that the beamstop not only effectively blocks the direct beam, but also the scattering at very small angles. Therefore, a small beamstop is generally desirable. By mounting a photon counting device, for example a diode, on the beamstop, it is possible to measure the X-ray attenuation simultaneously. This is of particular interest for inhomogeneous specimens, since also the scattered intensity is attenuated by the specimen. It is also directly proportional to specimen thickness. Thus, for a known wavelength λ the scattered intensity I is proportional to

$$I \propto I_0 \cdot t \cdot e^{-\mu t}, \quad (12.4)$$

where μ is the linear attenuation coefficient for the specimen at wavelength λ , I_0 and I are the incoming and scattered intensities, respectively, and t is the specimen thickness. The optimal specimen thickness, where the scattered intensity is maximal, corresponds to $t=1/\mu$ [6]. The specimen thickness should always be chosen so that the beam illuminates a reasonable volume. If the attenuation is known, the scattered intensity can be corrected by the specimen transmission.

The smallest angles, where a SAXS signal can be measured, is given by the size of the beamstop, which in return is determined by the cross sectional size of the

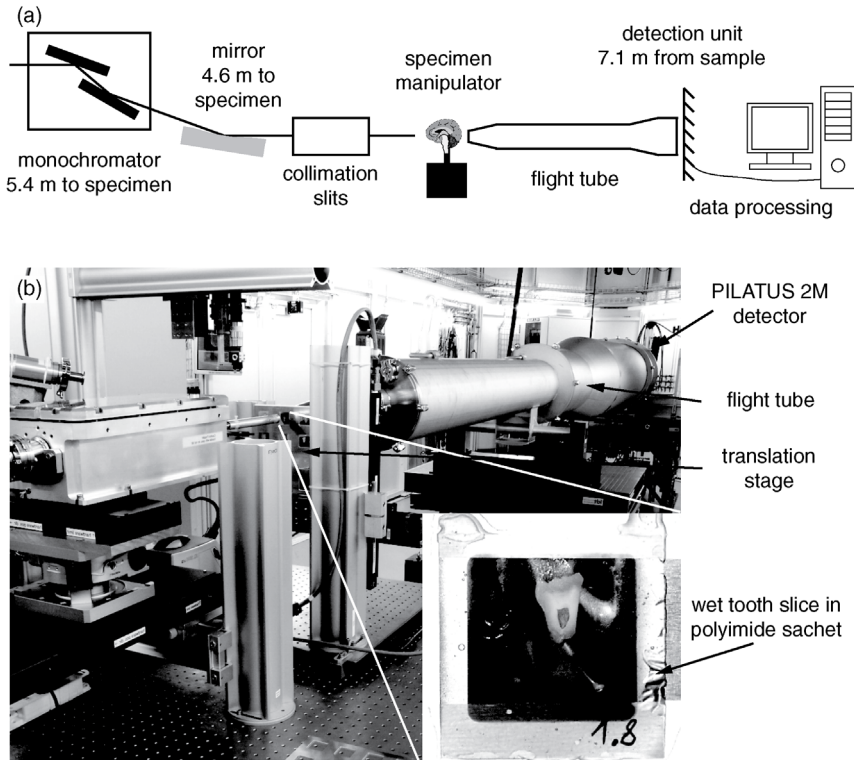


Figure 12.2 (a) Schematic representation of the cSAXS beamline at the Swiss Light Source, Villigen, Switzerland. (Adapted from Ref. [9]. With permission from Springer-Verlag Berlin Heidelberg.) (b) The end station of the cSAXS beamline at the Swiss Light Source, Villigen,

Switzerland. The tissue of interest, here a slice of a human tooth, can be kept under wet conditions at a predefined temperature. (Adapted from Ref. [9]. With permission from Springer-Verlag Berlin Heidelberg.)

direct beam. The small direct beam size is generally obtained with a system of collimation slits or pinholes, depending on setup, resulting in beam sizes generally below $200\ \mu\text{m}$ at the position of the specimen.

Figure 12.2a shows a schematic representation of the SAXS setup at the cSAXS beamline located at the Swiss Light Source storage ring (Paul Scherrer Institut, Villigen, Switzerland) [4]. The wavelength for the experiment is selected by a monochromator, and the beam is focused to about $20\ \mu\text{m} \times 20\ \mu\text{m}$ at the specimen location by the monochromator and a mirror. It is further collimated by a system of horizontal and vertical slits. The specimen is mounted on a motorized x - y -stage for positioning, and the scattered light is collected with a PILATUS single photon counting detector [8]. The direct beam is blocked by a beamstop in front of the detector, equipped with a proportional counting diode. A flight tube is placed between the specimen and the detector. It can be either

evacuated, or filled with inert gas, to minimize air scattering. Figure 12.2b shows a photograph of the end station.

In order to operate an efficient spatially resolved SAXS system, powerful personal computers and dedicated software are required.

12.2.3

Two-Dimensional Scanning Small-Angle X-Ray Scattering

SAXS measurements can be combined with two-dimensional scanning to obtain information on the nanometer range over macroscopic areas [4,5]. Then, the specimen, here the tissue of interest, is scanned in raster fashion through the beam by means of a motorized x - y -stage. A scattering pattern is acquired at each position, allowing creating a two-dimensional map over extended areas (cf. Figure 12.3). Depending on the actual set-up, one may need about 1 h beamtime to record an area of $1\text{ cm} \times 1\text{ cm}$ with a raster of $10\text{ }\mu\text{m} \times 10\text{ }\mu\text{m}$.

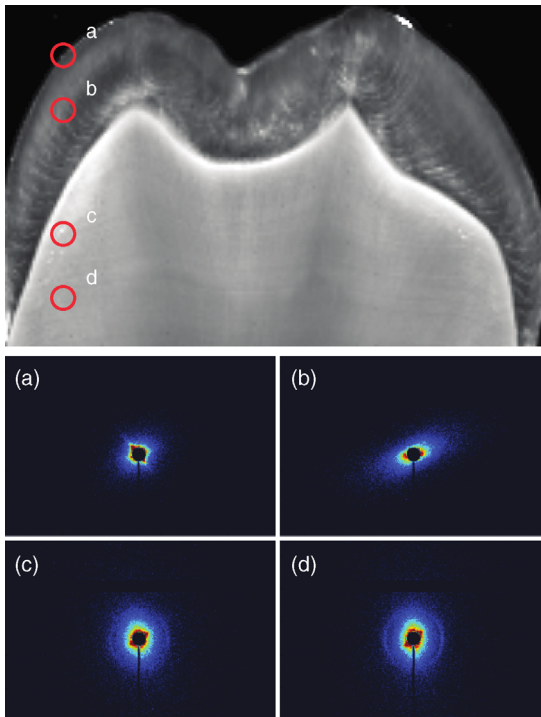


Figure 12.3 The tooth slice several hundred micrometer thick is scanned through the collimated X-ray beam in x and y directions (cf. Figure 12.2). At each position a SAXS

pattern is acquired, and nanoscale information is mapped over macroscopic areas. (Adapted from Ref. [10]. With permission from Springer Science+Business Media B.V.)

12.2.4

Scattering Pattern Analysis

After acquisition, the scattering pattern is further processed, integrating the intensity values in radial or azimuthal directions, as depicted in Figure 12.4. In practice, this is often performed by dividing the scattering patterns into radial segments, and averaging, in each segment, the intensity of all pixels with the same distance to the beam center [4]. Several bits of information can be extracted from the obtained curves. The radial plots, where the intensity I is plotted against the scattering angle, or the scattering vector q , holds information about shape and size distribution of the scattering features within the specimen [6,7]. Alternatively, preferential orientation and anisotropy of periodicities of special interest can be observed by plotting the SAXS intensity against the azimuthal position. If the scattering features exhibit one preferential orientation, the azimuthal plot will display two peaks, reflecting the central symmetry of the scattering pattern. The preferential orientation can be extracted from the peak position with respect to the vertical direction. Since the scattering signal is

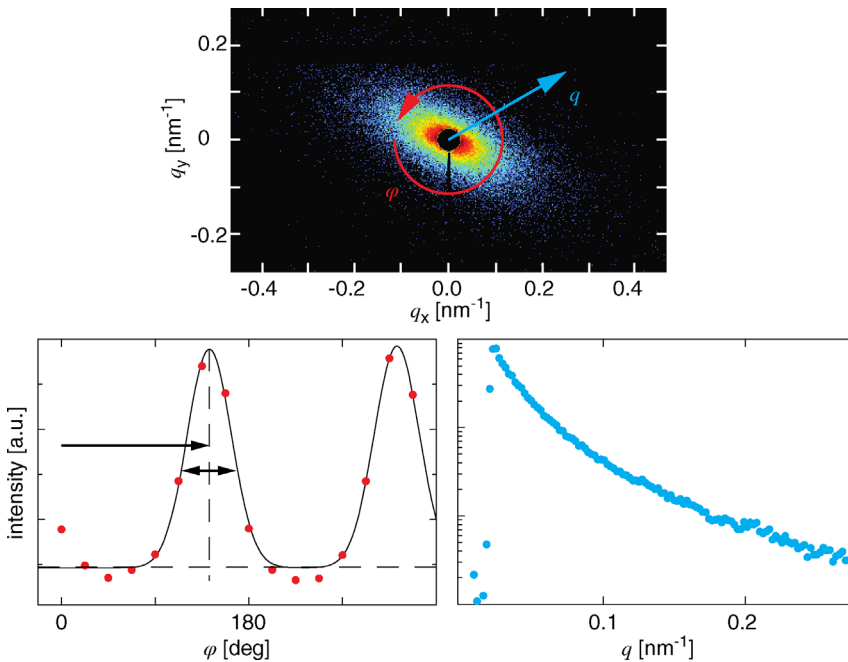


Figure 12.4 The two-dimensional SAXS pattern can be integrated radially along q or azimuthally along φ . The I versus q plot is linked to the shape and the size distribution of the scattering features within the specimen/tissue.

The azimuthal plot along φ provides information about specimen/tissue anisotropy. The q -values smaller than a certain cut-off are inaccessible because of the beamstop.

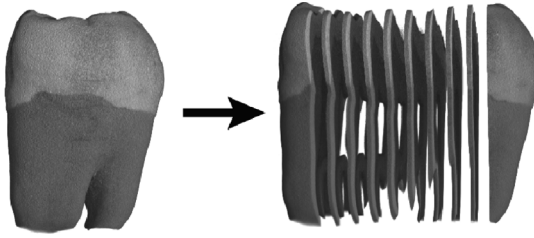


Figure 12.5 Serial sectioning of a human third molar into slices each about $500\ \mu\text{m}$ thin.

typically oriented perpendicular to the largest extension of structures like rods and platelets, the preferential orientation of these features can be deduced. A measure for the anisotropy and physical spread of the scattering nanofeatures can be deduced by analyzing the shape of the scattered intensity [5,11]. Thus, depending on the extracted information, several types of *contrast* can be obtained from a single SAXS measurement. Integration has the added benefit of drastically reducing data size. A thorough treatment and additional parameters can be found, for example, in references [4,12].

12.2.5

Tissue Preparation

As stated in Section 12.2.4, specimen thickness has to be carefully chosen prior to performing the experiment. For specimens from human tissues, generally having a size in the range of a few to several cm, this involves sectioning into thin slices.

Scattered intensity increases linearly with specimen thickness; therefore, thickness should be chosen appropriately to ensure sufficient signal. Scattered intensity is, however, also attenuated within the specimen, requiring the specimen to be thin enough so that a reasonable amount of photons reaches the detector. Furthermore, SAXS measurements are of projective nature, meaning that resolution is limited to the specimen thickness. This is of particular interest for human specimens, where changes on structural organization might happen in the micrometer range, or even below, or interfaces between adjacent tissues are present. Different structures overlapping along the beam will be projected on the same spot. Separating their contribution to the scattering pattern obtained in this manner is often infeasible and thus hinders data interpretation. The projective nature of the method also implies that sequential sectioning might be required to obtain information on volumetric specimens (cf. Figure 12.5).

It should also be noted that SAXS is generally only sensitive to features lying in the plane perpendicular to the direction \mathbf{k} of the incident X-ray beam, because for small scattering angles θ , the scattering vector \mathbf{q} is almost perpendicular to \mathbf{k} . The sectioning direction of the specimen is therefore crucial. Highly oriented

structures might remain invisible in the scattering pattern if the sectioning plane is inappropriately selected.

Since vacuum is not a necessary requirement for X-ray experiments, specimen environment can be chosen to best suit specimen specifications. For example, a wet environment can be realized by storing specimens in sachets (cf. Figure 12.2). Special care should be taken that the sachet material exhibits low and especially uniform scattering (cf. Section 12.6). For example, polyimide is routinely used at the cSAXS beamline to hold specimens wet during the measurements.

12.3

Nanoanatomy of Human Hard and Soft Tissues

12.3.1

Human Tooth

Figure 12.6 shows processed scanning SAXS data of a human tooth slice for the range corresponding to 60 and 70 nm. In Figure 12.6a, the total scattered intensity is represented, which is related to the abundance of periodicities in this nanometer range.

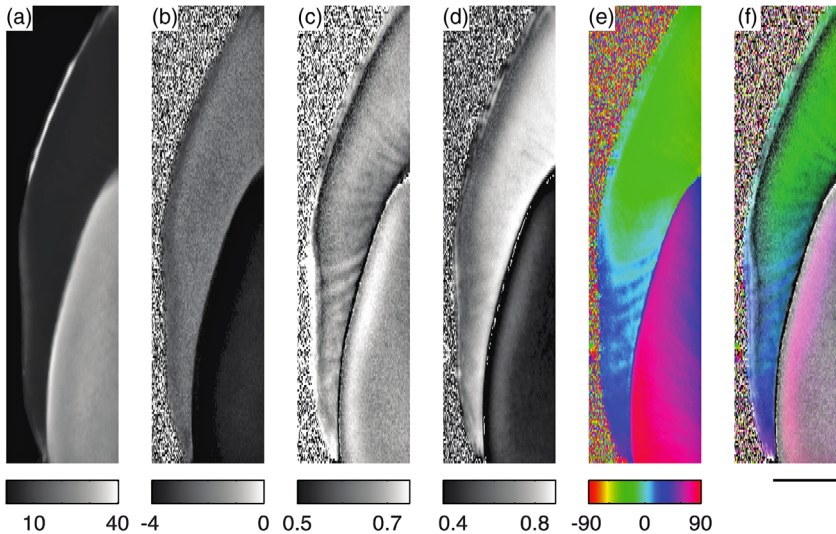


Figure 12.6 Several types of contrast can be extracted from the scattering patterns. (a) Total scattered intensity in counts per pixel.

(b) Intensity exponent. (c) FWHM of the azimuthal scattering distribution in radians.

(d) Anisotropy, that is, the amount of anisotropic scattering. (e) Preferential orientation of

the scattering signal with respect to the vertical direction. (f) Several contrast types can be combined within one image. Here, the color indicates the preferential orientation, the saturation gives the FWHM, or physical spread of the scatterers, and the intensity codes the anisotropy. The length bar corresponds to 1 mm.

Figure 12.6b displays the *intensity exponent* α , which is derived fitting the I - q curve with the power law q^α . The exponent α is linked to the shape of the scattering features, corresponding to -1 for needle and rod-like structures and to -2 for platelets and disks [7]. Note that this relationship is only valid for specific q -ranges dependent on the scattering feature sizes and for dilute solutions [6,7]. Therefore, these conditions are hardly met in the densely packed enamel and dentin. Nonetheless, the exponent allows distinguishing enamel from dentin, and even gives rise to contrast within certain regions of the enamel. The images of Figure 12.6c and d show some aspects of the anisotropy within the tooth crown. The image in Figure 12.6c relates to the physical spread of the scattering features, whereas the image in Figure 12.6d shows the ratio of oriented to total scattering. The alternating brighter and darker regions in enamel correspond to the Hunter-Schreger bands well known from optical micrographs [13]. They originate from bundles of coaligned enamel rods [14]. In enamel, the scattering features are almost exclusively oriented. They are more isotropic in dentin. The preferential orientation of the scattering signal is visualized in Figure 12.6e using the color code according to the bar. Zero means vertical orientation.

In order to provide the information to the viewer in concentrated manner, the contrast of selected representations are often combined. Figure 12.6f shows such an example, which is appreciated by medical experts including anatomists.

Each periodic structure gives rise to a related peak in the I - q plot. For example, the main organic component of dentin, collagen-I, exhibits periodic gap zones at the 67 nm spacing [15]. Figure 12.7a contains characteristic I - q diagrams for dentin (red color) and enamel (blue color). The first order collagen peak causes a bump in the curve for dentin. Such a peak is absent for enamel. The intensity below the bump can be approximated with a power law q^α with $\alpha = -2.6$. Then, the intensity above the fit is exclusively associated with the occurrence of collagen-I [16], which can be processed separately. The associated results are given in the images of Figure 12.7b and d. Here, the scattering potential is coded by brightness, anisotropy by color saturation, and preferential orientation of the scattering signal by color according to the color wheel. In Figure 12.7b, the total intensity was processed, which mainly originates from the inorganic components [16]. The preferential orientation of the scattering signal in enamel is mostly parallel to the dentin-enamel junction (DEJ), whereas in dentin it is perpendicularly oriented. In Figure 12.7d, only the collagen-related intensity is displayed. In dentin, the preferential orientation of the collagen-related scattering signal is perpendicular to the one originating from the inorganic components, indicating a close organizational relation between these essential components.

The investigated q -range can be shifted to higher values by reducing the specimen-detector distance (cf. Figure 12.8). In this regime, termed wide-angle X-ray scattering (WAXS), diffraction patterns of crystallites can be accessed. Figure 12.9 shows spatially resolved WAXS data of a selected human tooth slice. Since the main inorganic component of the crown is hydroxyapatite, most peaks can be associated to this lattice structure. Similarly to SAXS data processing, the

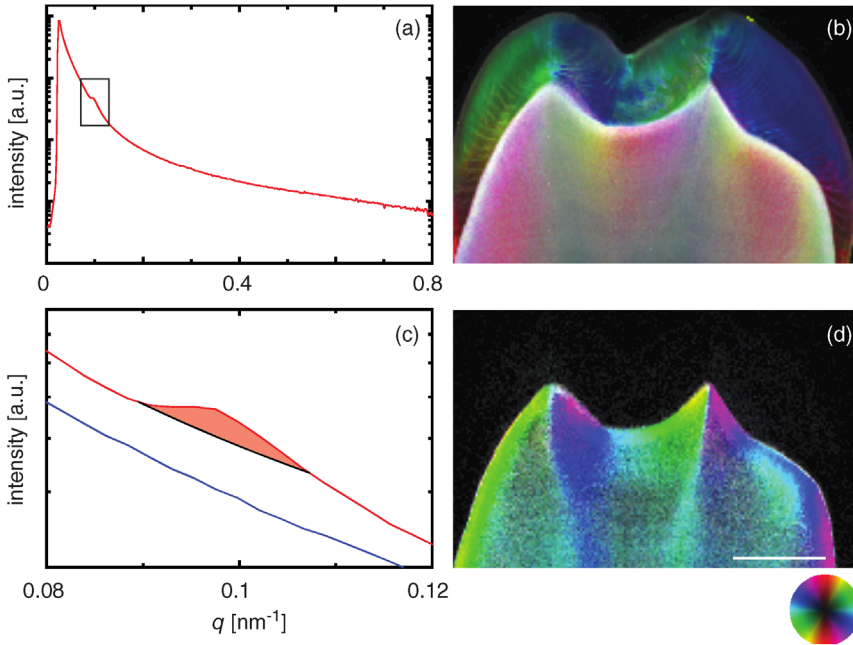


Figure 12.7 The diagram (a) shows characteristic scattering curves of dentin in red color and of enamel in blue color. The image (b) is the locally processed SAXS signal, where the orientation of the scattering signal is according to the color-wheel, scattering potential is coded by brightness, and anisotropy by color

saturation. The distinct periodicity of about 67 nm in the collagen fibers gives rise to a related peak in the scattering signal (c). This signal, related to collagen-I, can be extracted and allows generating descriptive images as displayed in (d). The scale bar corresponds to a length of 2 mm.

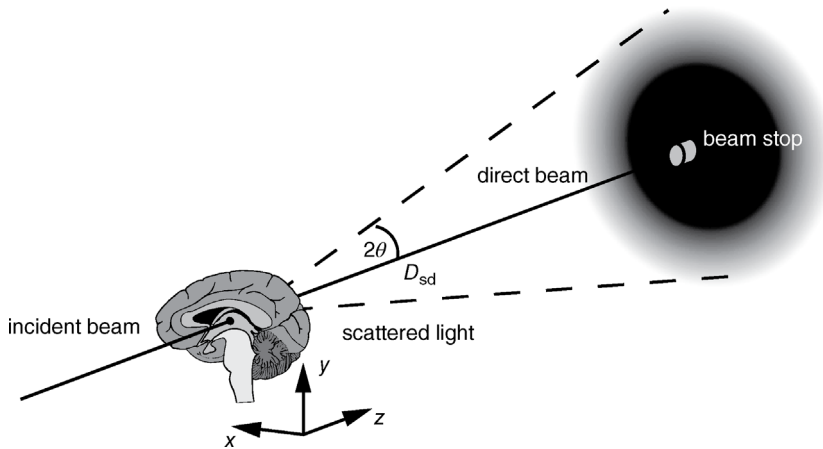


Figure 12.8 Schematic representation of a standard scattering measurement setup. A collimated X-ray beam impinges on the tissue of interest. The scattered X-rays are collected on a detector, whereas the transmitted radiation is absorbed at the beam stop.

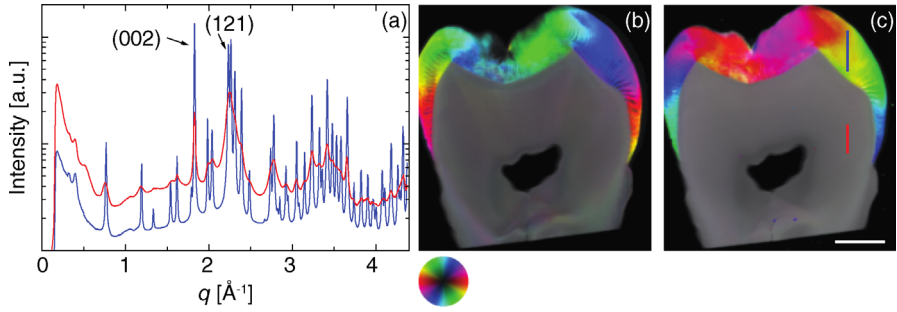


Figure 12.9 The diagram (a) reveals the characteristic diffraction (WAXS) patterns of enamel in blue color and of dentin in red color. Most of the peaks are easily associated to hydroxyapatite. The images (b) and (c) present the locally processed signals of the (002) and (121) planes, respectively. The color corresponds to the orientation of the diffraction peak according to the color-wheel, whereas the color saturation indicates anisotropy in the plane of the specimen. The scale bar corresponds to a length of 2 mm.

intensity associated with individual peaks can be processed, as performed here for the families of (002) and (121) planes and depicted in the images of Figure 12.9b and c, respectively. In enamel, the (002) signal orients radially to the DEJ. The (121) signal is oriented parallel to the DEJ. The comparison with SAXS data reveals that the (002) direction, corresponding to the *c*-axis, aligns with the long axis of the needle-shaped crystallites. No distinct orientation can be identified for dentin.

The anatomical knowledge on the nanometer scale should be applied for the realization of nature-inspired, biomimetic fillings. Currently, the dentists repair caries lesions mechanically removing the affected parts of the crown and filling the cavity using advanced isotropic materials. These dental fillings usually do not reach the duration of the natural counterpart. Consequently, dental fillings should be inserted, which contain elongated nanostructures with the orientation of dentin and enamel [17].

The study of caries pathology using synchrotron radiation-based hard X-ray scattering has demonstrated that while bacterial processes do dissolve the ceramic components in enamel and dentin, the dentinal collagen network remains unaffected, enabling the development of future caries treatments that remineralize the dentin [16].

12.3.2

Femoral Head

The articular cartilage of the human femoral head is composed of layered tissues, as schematically depicted in Figure 12.10b [18]. This configuration illustrates the tissue's function as load bearing and shock absorbing anatomical structure [19,20]. Applying the two-dimensional position-resolved SAXS, it is possible to map the local orientation of collagen fibrils from the femoral head

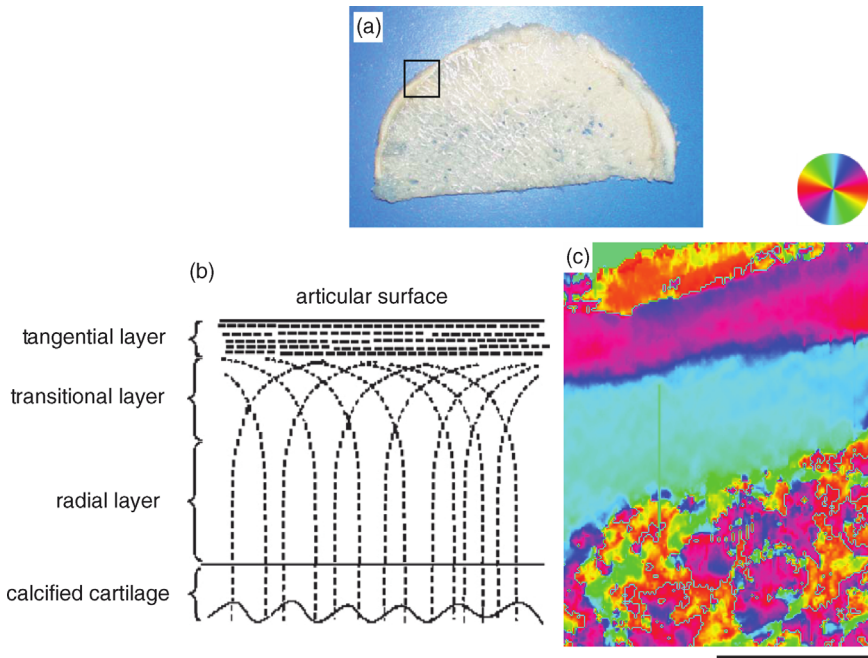


Figure 12.10 The rectangle of the photograph (a) indicates the area of a section of decalcified femoral head selected for the scanning SAXS measurement. The scheme (b) shows the anatomical layered structure from the bone to the articular surface indicating the alignment of collagen fibers in knee cartilage. The spatially resolved SAXS data shown in the image (c) reveals the main orientation of the scattering signal in the range from 12.5 to

13.7 nm according to the color-wheel. The orientation of the signal changes from parallel to perpendicular to the surface. These data show results from the first scanning SAXS experiments performed at the cSAXS beamline in August 2007. The length bar corresponds to 500 μm . (Adapted from Ref. [18]. With permission from Elsevier.) (Adapted from Ref. [19]). With permission from Elsevier. SAXS data with permission by D. Bradley.)

surface down to the underlying subchondral plate and the trabecular bone. The SAXS data reveal the parallel alignment of the collagen fibers at the articular surface, which accommodate the gliding motion of the joint, then a change to a perpendicular arrangement in the direction of mechanical loading [19,21]. Such measurements can, for example, be utilized to track osteoarthritis, that is, the induced changes of the anatomy on the nanometer scale in affected joints, *ex vivo* [19].

Currently, the repair of joints is only partially possible. Once the joint, such as hip and knee, is severely damaged, it is replaced using medical implants. Although this surgical treatment is a standard medical procedure, rather complex complications can occur. Therefore, tissue engineering is still an interesting alternative. Related research activities are ongoing. The spatially resolved SAXS data underline the necessity (i) to incorporate anisotropic nanostructures into

the tissue-engineered constructs and (ii) to extend the two-dimensional arrangements of biological cells into the third dimension. Here, one finds some promising results concerning bone substitutes [22]. Nevertheless, the tissue engineering of joints is still at the very early stage of development. Research initiatives with durations of rather a decade than a year will be required to build the tissues in a biomimetic manner with ordered anisotropic nanostructures as revealed with the spatially resolved SAXS measurements.

12.3.3

Breast Tumor

In order to diagnose breast cancer, medical experts have to discriminate between normal tissue and benign as well as malignant lesions. This task is often challenging. The result has major impact on the survival and the quality of life of the affected patients. It has been demonstrated that SAXS allows classifying formalin-fixed human breast tissues as normal, benign, or malignant with a high sensitivity and specificity [23–28]. Here, the scientists have analyzed both the Bragg peaks of the collagen fibrils and the scattering of the packing of triglycerides in the lamellar phase present in normal tissue. Usually, several parameters are derived to improve the significance. Figure 12.11, for example, shows beside the histology slice, the related, simultaneously obtained spatially resolved SAXS data for the degree of orientation, the intensity exponent, the total scattered intensity, and the preferential orientation of the scattering signal corresponding to the range between 6 and 21 nm. One easily recognizes the similarities between conventional histology and spatially resolved SAXS data as well as the additional information SAXS can provide with respect to the conventional approach. Although laboratory set-ups are sufficient to discriminate the cancerous and healthy parts of the breast tissues, further efforts have to be invested to develop spatially resolved SAXS toward mammography screening.

12.3.4

Brain Tissue

Brain tissue contains prominent nanoscale periodicities, which include the myelin sheaths that surround the nerve axons. They have a spiral arrangement with a constant separation distance between the turns of about 17 nm and act as electrical isolation. Similar to collagen, this 17 nm periodicity gives rise to distinct peaks in the $I-q$ plots. Degenerative pathological events can alter its abundance and structure [29]. The images of Figure 12.12a and b show the total and myelin-related signals of a human brain slice. The image represented in Figure 12.12c depicts the relative frequency of the myelin signal. The central dark region belongs to the thalamus, where the myelin is hardly found. Around the thalamus, however, abundant myelin sheaths, that surround the nerve axons, are present.

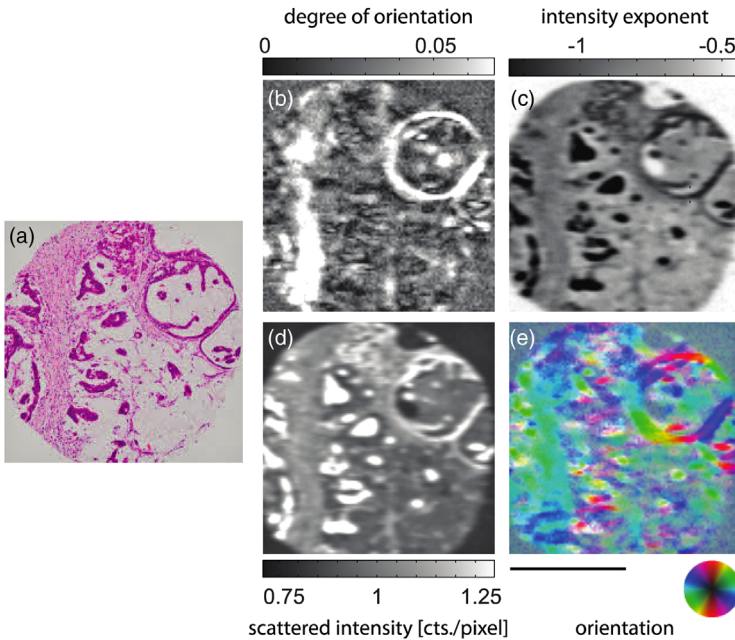


Figure 12.11 (a) Histology slice of human breast tissue. (b) Degree of orientation. (c) Intensity exponent. (d) Total scattered intensity. (e) Orientation of the scattering signal, according to the color-wheel. The

nanostructures in the range from 6 to 21 nm are considered. The scale bar corresponds to a length of 500 μm. Histology and SAXS data with permission by D. Bradley.

The two-dimensional SAXS measurements can be extended to the third dimension incorporating a rotation, for example, around y -axis (cf. Figure 12.2). In this manner, SAXS is combined with a tomographic setup. The well-known reconstruction schemes, that is, filtered back-projection, can be applied. The direction-dependent nature of the SAXS signal imposes limitations on the information that is obtained. The scattering intensity signal, related to the abundance of nanostructures, can only be meaningfully reconstructed, if the nanostructures are isotropic, meaning that scattered intensity is independent on specimen's orientation [30–32]. Using this method the preferential orientation of the scattering features cannot be reconstructed. Nonetheless, this basic approach can result in a remarkable contrast, as shown in the images of Figure 12.12d and e for rat brain. The images, displayed in Figure 12.12d and g, show conventional tomography slices in absorption-contrast mode. Only a few features can be identified. Conversely, improved contrast is found in the SAXS-CT data that are displayed in the images of Figure 12.12e and h. Similar to the two-dimensional data, the intensity associated with myelin can be processed and reconstructed separately, allowing for the access of the myelin density in each voxel [31]. These unique results are visible in the images of Figure 12.12f and i.

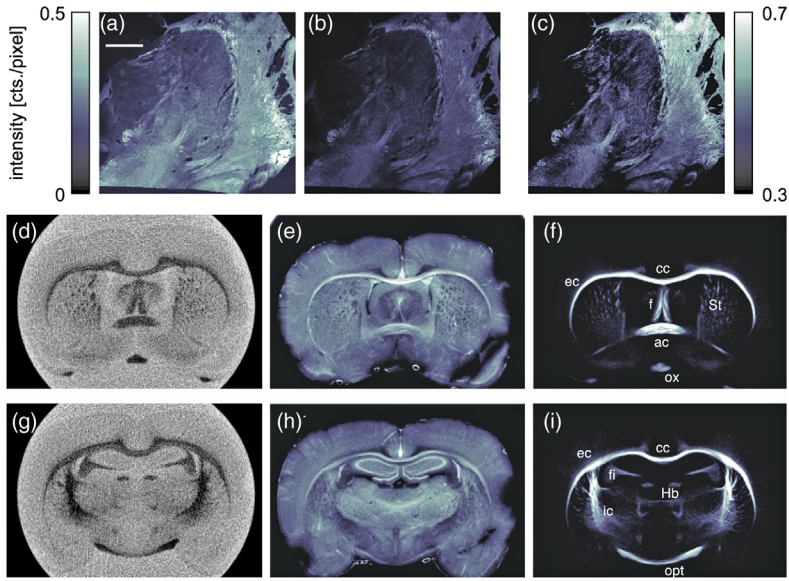


Figure 12.12 In the top row (a) two-dimensional SAXS intensity of a histology slice from the human thalamus for the range between 8.2 and 9.0 nm. (b) Myelin-related signal. (c) Ratio of the images represented in (b) and (a), giving rise to the relative myelin abundance. The scale bar corresponds to a length of 5 mm. In the second and third row, one finds selected tomographic slices of SAXS-CT data

reconstructed by filtered back-projection from a rat brain. (d) and (g) absorption contrast. (e) and (h) total scattering signal. (f) and (i) myelin-related signal. The scale bar corresponds to a length of 2 mm. ((d, g) Adapted from Ref. [30], with permission from IOP Publishing. (e, f, h, i) Adapted from Ref. [31], with permission from Elsevier.)

For specimens presenting a high degree of anisotropy on the nanometer scale the approach is, however, questionable, and more sophisticated measurements and reconstruction algorithms have to be developed. Very recently, Georgiadis *et al.* have proposed a method for the three-dimensional assessment of the local orientation of nanocomponents of bone using spatially resolved SAXS [33]. This method relies on the inspection of thin slices in a similar manner as for the projection approach in spatially resolved SAXS. Here, however, the measurement is repeated for a variety of incidence angles with respect to the beam, allowing for the reconstruction of the local preferential orientation of the nanostructures in three dimensions. As for the two-dimensional projection data, the spatial resolution is limited to the slice thickness. To investigate volumetric specimen, sequential sections can be scanned, as performed successfully for bone [33].

The two- and three-dimensional SAXS data allow for a detailed evaluation of brain tissues in health and disease. Based on the present results, the future SAXS experiments will expand our understanding of neurodegenerative diseases and the role of the nanostructures and their arrangement for the well and fit aging.

12.4

Conclusions and Outlook

Our body can be regarded as the arrangement of atomic and molecular species in hierarchical manner to offer the dedicated functionality. Radiologists, however, cannot resolve the individual atoms and molecules, because the spatial resolution of their modalities is not better than a fraction of a millimeter. Specialized computed tomography based on hard X-rays can reach the sub-micrometer level for specimens of a restricted size. Atoms and molecules within biopsies, however, are inaccessible so far. As a consequence, the diffraction- and scattering-based, k -space techniques are extremely helpful. We have known these techniques in the fields of crystallography, physics, and materials science for about a century. The detailed understanding of these methods, however, is demanding. More recently, however, the scattering techniques have been combined with scanning in two dimensions taking advantage of well-collimated hard X-ray beams. In this way, images of a reasonable tissue area with strong similarities with histology can be generated. In comparison with histology, however, staining procedures can be avoided, which allows investigations closer to the physiological stage. Even more important, SAXS permits the determination of the orientation and degree of anisotropy of the nanoscale ultrastructure that is impossible using conventional histology. This feature is essential, since the human tissues are almost exclusively anisotropic. The combination with tomographic reconstruction is still in its infancy and restricted to rather small volumes.

SAXS has been successfully applied to a variety of hard and soft tissues [21]. Diseases can be diagnosed even in quantitative manner. The results may be applied to develop next-generation treatment strategies, as, for example, being demonstrated for caries [16].

References

- 1 White, S.N., Luo, W., Paine, M.L., Fong, H., Sarikaya, M., and Snead, M.L. (2001) Biological organization of hydroxyapatite crystallites into a fibrous continuum toughens and controls anisotropy in human enamel. *J. Dent. Res.*, **80** (1), 321–326.
- 2 Lareida, A., Beckmann, F., Schrott-Fischer, A., Glueckert, R., Freysinger, W., and Müller, B. (2009) High-resolution X-ray tomography of the human inner ear: synchrotron radiation-based study of nerve fiber bundles, membranes, and ganglion cells. *J. Microsc.*, **234** (1), 95–102.
- 3 Schulz, G., Weitkamp, T., Zanette, I., Pfeiffer, F., Beckmann, F., David, C., Rutishauser, S., Reznikova, E., and Müller, B. (2010) High-resolution tomographic imaging of a human cerebellum: comparison of absorption and grating based phase contrast. *J. R. Soc. Interface*, **7** (53), 1665–1676.
- 4 Bunk, O., Bech, M., Jensen, T.H., Feidenhans'l, R., Binderup, T., Menzel, A., and Pfeiffer, F. (2009) Multimodal x-ray scatter imaging. *New J. Phys.*, **11**, 123016.
- 5 Fratzl, P., Jakob, J.F., Rinnerthaler, S., Roschger, P., and Klaushofer, K. (1997) Position-resolved small-angle X-ray

- scattering of complex biological materials. *J. Appl. Crystallogr.*, **30**, 765–769.
- 6 Glatter, O. and Kratky, O. (eds) (1982) *Small-Angle X-ray Scattering*, Academic Press, London.
 - 7 Guinier, A. and Fournet, G. (eds) (1955) *Small Angle Scattering of X-rays*, John Wiley & Sons, Inc., New York.
 - 8 Kraft, P., Bergamaschi, A., Broennimann, C., Dinapoli, R., Eikenberry, E.F., Henrich, B., Johnson, I., Mozzanica, A., Schlepütz, C.M., Willmott, P.R., and Schmitt, B. (2009) Performance of single-photon-counting PILATUS detector modules. *J. Synchrotron Radiat.*, **16**, 368–375.
 - 9 Schulz, G. *et al.* (2012) Imaging the human body: micro- and nanostructure of human tissues, in *NanoScience and Technology* (ed. S. Logothetidis), Springer-Verlag Berlin Heidelberg.
 - 10 Deyhle, H. *et al.* (2012) Imaging the human body down to the molecular level, in *Encyclopedia of Nanotechnology* (eds B. Bhushan and H.D. Winbigler), Springer Science+Business Media B.V.
 - 11 Deyhle, H., White, S.N., Bunk, O., Beckmann, F., and Müller, B. (2014) Nanostructure of the carious tooth enamel lesion. *Acta Biomater.*, **10** (1), 355–364.
 - 12 Pabisch, S., Wagermaier, W., Zander, T., Li, C., and Fratzl, P. (2013) Imaging the nanostructure of bone and dentin through small- and wide-angle X-ray scattering, in *Methods in Enzymology, Research Methods in Biomineralization Science* (ed. J.J. De Yoreo), Academic Press, pp. 391–413.
 - 13 Gaiser, S., Deyhle, H., Bunk, O., White, S.N., and Müller, B. (2012) Understanding nano-anatomy of healthy and carious human teeth: a prerequisite for nanodentistry. *Biointerphases*, **7**, 4.
 - 14 Mortell, J.F. and Peyton, F.A. (1956) Observation of Hunter-Schreger bands. *J. Dent. Res.*, **35** (5), 804–823.
 - 15 Kinney, J.H., Pople, J.A., Marshall, G.W., and Marshall, S.J. (2001) Collagen orientation and crystallite size in human dentin: a small angle X-ray scattering study. *Calcif. Tissue Int.*, **69**, 31–27.
 - 16 Deyhle, H., Bunk, O., and Müller, B. (2011) Nanostructure of healthy and caries-affected human teeth. *Nanomed. Nanotech. Biol. Med.*, **7**, 694–701.
 - 17 Deyhle, H., Bunk, O., Buser, S., Krastl, G., Zitzmann, N., Ilgenstein, B., Beckmann, F., Pfeiffer, F., Weiger, R., and Müller, B. (2009) Bio-inspired dental fillings. *Proc. of SPIE*, **7401**, 74010E 11.
 - 18 Kaabar, W., Daar, E., Gundogdu, O., Jenneson, P.M., Farquharson, M.J., Webb, M., Jaynes, C., and Bradley, D.A. (2009) Metal deposition at the bone-cartilage interface in articular cartilage. *Appl. Radiat. Isot.*, **67**, 475–479.
 - 19 Kaabar, W., Gundogdu, O., Laklouk, A., Bunk, O., Pfeiffer, F., Farquharson, M.J., and Bradley, D.A. (2010) μ -PIXE and SAXS studies at the bone-cartilage interface. *Appl. Radiat. Isot.*, **68**, 730–734.
 - 20 Stockwell, R.A. (ed.) (1970) *Biology of Cartilage Cells*, vol. 7, Cambridge University Press, New York.
 - 21 Müller, B., Deyhle, H., Bradley, D., Farquharson, M., Schulz, G., Müller-Gerbl, M., and Bunk, O. (2010) Scanning x-ray scattering: evaluating the nanostructure of human tissues. *Eur. J. Clin. Nanomed.*, **3**, 30–33.
 - 22 Hoffmann, W., Bormann, T., Rossi, A., Müller, B., Schumacher, R., Martin, I., de Wild, M., and Wendt, D. (2014) Rapid prototyped porous nickel–titanium scaffolds as bone substitutes. *J. Tissue Eng.*, **5**, 1–14.
 - 23 Conceicao, A.L., Antoniassi, M., and Poletti, M.E. (2009). Analysis of breast cancer by small angle X-ray scattering (SAXS). *Analyst*, **134** (6), 1077–1082.
 - 24 Falzon, G., Pearson, S., Murison, R., Hall, C., Siu, K., Evans, A., Rogers, K., and Lewis, R. (2006) Wavelet-based feature extraction applied to small-angle x-ray scattering patterns from breast tissue: a tool for differentiating between tissue types. *Phys. Med. Biol.*, **51** (10), 2465–2477.
 - 25 Fernandez, M., Keyrilainen, J., Serimaa, R., Torkkeli, M., Karjalainen-Lindsberg, M.L., Leidenius, M., von Smitten, K., Tenhunen, M., Fiedler, S., Bravin, A., Weiss, T.M., and Suortti, P. (2005) Human breast cancer *in vitro*: matching histo-pathology with small-angle x-ray scattering and diffraction enhanced x-ray imaging. *Phys. Med. Biol.*, **50** (13), 2991–3006.
 - 26 Fernandez, M., Keyrilainen, J., Serimaa, R., Torkkeli, M., Karjalainen-Lindsberg, M.L.,

- Tenhunen, M., Thomlinson, W., Urban, V., and Suortti, P. (2002) Small-angle x-ray scattering studies of human breast tissue samples. *Phys. Med. Biol.*, **47** (4), 577–592.
- 27 Round, A.R., Wilkinson, S.J., Hall, C.J., Rogers, K.D., Glatter, O., Wess, T., and Ellis, I.O. (2005) A preliminary study of breast cancer diagnosis using laboratory based small angle x-ray scattering. *Phys. Med. Biol.*, **50** (17), 4159–4168.
- 28 Sidhu, S., Siu, K.K.W., Falzon, G., Nazaretian, S., Hart, S.A., Fox, J.G., Susil, B.J., and Lewis, R.A. (2008) X-ray scattering for classifying tissue types associated with breast disease. *J. Med. Phys.*, **35** (10), 4660–4670.
- 29 De Felici, M., Felici, R., Ferrero, C., Tartari, A., Gambaccini, M., and Finet, S. (2008) Structural characterization of the human cerebral myelin sheath by small angle x-ray scattering. *Phys. Med. Biol.*, **53**, 5675–5688.
- 30 Jensen, T.H., Bech, M., Bunk, O., Thomsen, M., Menzel, A., Bouchet, A., LeDuc, G., Feidenhans'l, R., and Pfeiffer, F. (2011) Brain tumor imaging using small-angle x-ray scattering tomography. *Phys. Med. Biol.*, **56**, 1717–1726.
- 31 Jensen, T.H., Bech, M., Bunk, O., Menzel, A., Bouchet, A., LeDuc, G., Feidenhans'l, R., and Pfeifer, F. (2011) Molecular x-ray computed tomography of myelin in a rat brain. *Neuroimage*, **57** (1), 124–129.
- 32 Schroer, C.G., Kuhlmann, M., Roth, S.V., and Gehrke, R. (2006) Mapping the local nanostructure inside a specimen by tomographic small-angle x-ray scattering. *Appl. Phys. Lett.*, **88**, 164102.
- 33 Georgiadis, M., Guizar-Sicairos, M., Zwahlen, A., Trüssel, A.J., Bunk, O., Müller, R., and Schneider, P. (2015) 3D scanning SAXS: A novel method for the assessment of bone ultrastructure orientation. *Bone*, **71**, 42–52.